Research article

Moritz Gittinger, Katja Höflich, Vladimir Smirnov, Heiko Kollmann, Christoph Lienau* and Martin Silies*

Strongly coupled, high-quality plasmonic dimer antennas fabricated using a sketch-and-peel technique

https://doi.org/10.1515/nanoph-2019-0379
Received September 20, 2019; revised October 31, 2019; accepted November 8, 2019

Abstract: A combination of helium- and gallium-ion beam milling together with a fast and reliable sketch-and-peel technique is used to fabricate gold nanorod dimer antennas with an excellent quality factor and with gap distances of less than 6 nm. The high fabrication quality of the sketch-and-peel technique compared to a conventional ion beam milling technique is proven by polarisation-resolved linear dark-field spectromicroscopy of isolated dimer antennas. We demonstrate a strong coupling of the two antenna arms for both fabrication techniques, with a quality factor of more than 14, close to the theoretical limit, for the sketch-and-peel–produced antennas compared to only 6 for the conventional fabrication process. The obtained results on the strong coupling of the plasmonic dimer antennas are supported by finite-difference time-domain simulations of the light-dimer antenna interaction. The presented fabrication technique enables the rapid fabrication of large-scale plasmonic or dielectric nanostructures arrays and metasurfaces with single-digit nanometer scale milling accuracy.

Keywords: helium-ion beam lithography; sketch and peel; plasmonic nanostructures; single-particle dark-field spectroscopy; strong coupling; quality factor; near-field enhancement.

***Corresponding authors: Christoph Lienau and Martin Silies,** Institute of Physics and Center of Interface Science, Carl von Ossietzky Universität Oldenburg, D-26129 Oldenburg, Germany, e-mail: christoph.lienau@uni-oldenburg.de. https://orcid.org/0000-0003-3854-5025 (C. Lienau); martin.silies@uni-oldenburg.de. https://orcid.org/0000-0002-3704-2066 (M. Silies)
Moritz Gittinger, Vladimir Smirnov and Heiko Kollmann: Institute of Physics and Center of Interface Science, Carl von Ossietzky Universität Oldenburg, D-26129 Oldenburg, Germany
Katja Höflich: Helmholtz Zentrum für Materialien und Energie Berlin, Hahn-Meitner-Platz 1, D-14109 Berlin, Germany; and Ferdinand-Braun-Institut, Leibniz-Institut für Höchstfrequenztechnik, Berlin, Germany. https://orcid.org/0000-0003-4088-2928

1 Introduction

Plasmonic nanostructures such as metallic nanoantennas act as functional elements in a wide range of applications. The intense evanescent electric field at the air–metal interface allows for the generation of 2-photon-photoluminescence [1–3], second [4–8], or third [9–12] harmonic and of femtosecond electron pulses [13, 14]. The spatial localisation of the electric field down to dimensions of the plasmonic nanostructure, i.e. to subwavelength dimensions, is accompanied by a dramatic field enhancement, which can then be employed in single-molecule spectroscopy [15, 16], scanning near-field microscopy [17], or electron steering processes [18, 19]. When arranged in groups of plasmonic particles such as bowtie [1, 9, 20, 21] or rod [20–22] dimer antennas, both the enhancement and the spatial confinement of the electric field can be boosted significantly, thanks to the growth of near-field–mediated optical interactions [23–25]. The electromagnetic coupling of the dimer antenna results in the hybridisation of the surface plasmon resonances (SPRs) of the monomers, forming an optically bright bonding mode and a dark, antibonding mode [26–30]. In this hybridisation model, the coupling strength and therefore the energy splitting of the two modes strongly increase with decreasing gap size [31, 32]. When this resonance shift $\delta\lambda$ exceeds the linewidth $\Delta\lambda$ of the linear optical resonance, i.e. $\delta\lambda/\Delta\lambda > 1$, the two antennas are referred to be strongly coupled. Here, the energy dissipation is smaller than the coupling, resulting in a periodic transfer of energy between both antenna arms [33, 34]. In order to reach this strong coupling regime in the field of plasmonics, special emphasis was put on the precise fabrication of the few-nanometer feed gaps between the metallic nanostructures. For bottom-up fabrication processes, single-molecular layer gaps

between a gold nanosphere and a metallic substrate could be achieved, recently reaching an anomalously large spectral shift near the quantum tunnelling regime [35, 36]. However, the ability to precisely shape the nanostructures is limited with this approach. Top-down lithography processes such as photo-resist–based electron-beam lithography (EBL) [12, 20, 24] provide high flexibility in controlling the shape of the nanoparticles and typically achieve gap sizes of slightly below 20 nm, limited by the proximity effect due to the backscattered electrons interacting with the sample [37]. Under optimized conditions [38, 39] or with overexposure techniques [40], gap sizes down to the single-digit nanometer level were accomplished. However, EBL is a sequential process, requiring several processing steps before the final device is created. Ga-based focused ion beam (Ga-FIB) milling procedures [27, 41, 42], in contrast, are limited by the finite focusing properties of the Ga^+-ion beam. Furthermore, undesired Ga^+-ion implantation into the sample as well as amorphisation of the nanostructure edges can furthermore significantly increase the linewidth of the longitudinally polarized SPR (LSPR) [43–46]. As a consequence, the quality factor Q of the antenna, defined as the ratio between the centre wavelength λ_0 and its linewidth $\Delta\lambda_{FWHM}$ taken as the full width at half maximum (FWHM), decreases considerably compared to the theoretical limit given by the frequency-dependent dielectric function of the structured materials. Hence, strongly coupled metallic nanostructures are difficult to realize using top-down processes such as EBL or Ga-FIB.

Recently, He^+-ion–based lithography (He-FIB) was introduced as a fabrication method to achieve gap sizes well below the 10-nm regime [9, 47–49]. Here, He^+ ions instead of Ga^+ ions are applied for the precise milling of plasmonic nanostructures in a smooth, single-crystalline metallic film [9, 48, 50]. As a distinct advantage, a much reduced line broadening of the plasmon resonances is observed when using He-FIB instead of Ga-FIB. The improved milling accuracy, however, comes at the cost of a significantly reduced milling speed due to the smaller ion mass compared to gallium. At higher ion doses, the ion bombardment can lead to an undesired implantation of helium at the substrate–metal interface [51]. To overcome this issue, Chen et al. [52] introduced a simple, fast, and reliable fabrication technique called “sketch and peel”–based FIB milling (SaP). In this process, a FIB at an appropriate dose is used to sketch only the outline of the desired plasmonic nanostructure to completely separate the particle and the rest of the film. In a second step, an adhesive tape is adhered onto the metallic surface and then peeled off from the substrate, resulting in dimer metallic particles with gap distances down to 20 nm. The key of this approach is that the surrounding metallic film can be selectively removed while the isolated plasmonic structures remain on the substrate during the peeling process.

In this work, we further optimize this approach and propose a combination of Ga-FIB, for the rough outlining, with He-FIB lithography, for the precise fabrication of the gap region of the dimer antenna, together with the SaP technique for the lift-off process. By using this combination, a reduction of the minimum gap size of down to 5 nm was achieved. We find a significant red shift of the LSPR of more than 150 nm for gap sizes of down to 5 nm accompanied with an outstanding quality factor of up to 14, proving the fabrication of low-loss plasmonic nanoresonators with performances approaching the theoretical limit.

The proposed SaP technique can fabricate large-size arrays of plasmonic structures without losing the fabrication speed or the nanometer-milling accuracy. Hence, this technique enhances the current capability of FIB lithography for the fabrication of metallic structures and therefore can bring the fabrication of large structures or large arrays of nanostructures with nanometer precision in a resistless and solvent-free way into reach.

2 Results and discussions

2.1 Sample preparation

Gold films with a thickness of 30 nm were deposited on a fused silica substrate using an electron-beam physical vapour evaporation process at a rate of 0.26 nm/s at a pressure of 8×10^{-6} mbar. The grain size of the polycrystalline gold films was increased in an annealing process at a temperature of 350°C for 8 h. The annealing process enlarges the typical size of single-crystalline grains from about 50 nm to 500 nm in diameter. Ion beam milling was performed by using both focused Ga^+ ions (Ga-FIB) in a dual-beam microscope (FEI Helios Nanolab 600i) and focused He^+ ions (He-FIB) in a He/Ne ion microscope (Zeiss Orion NanoFab).

Figure 1 depicts the three different strategies applied to fabricate pairs of gold nanorods with dimensions of $90\times35\times30$ nm^3 and with gap distances ranging from 5 to 35 nm. The rod length was chosen to match the LSPR of the long axis of the particle with the measuring range of our laser source and spectrometer. The rod width of 35 nm is limited by the fabrication process of the Ga^+-ion beam. The distance between two dimers was set to 3 μm, large enough to selectively image isolated dimer antennas in the

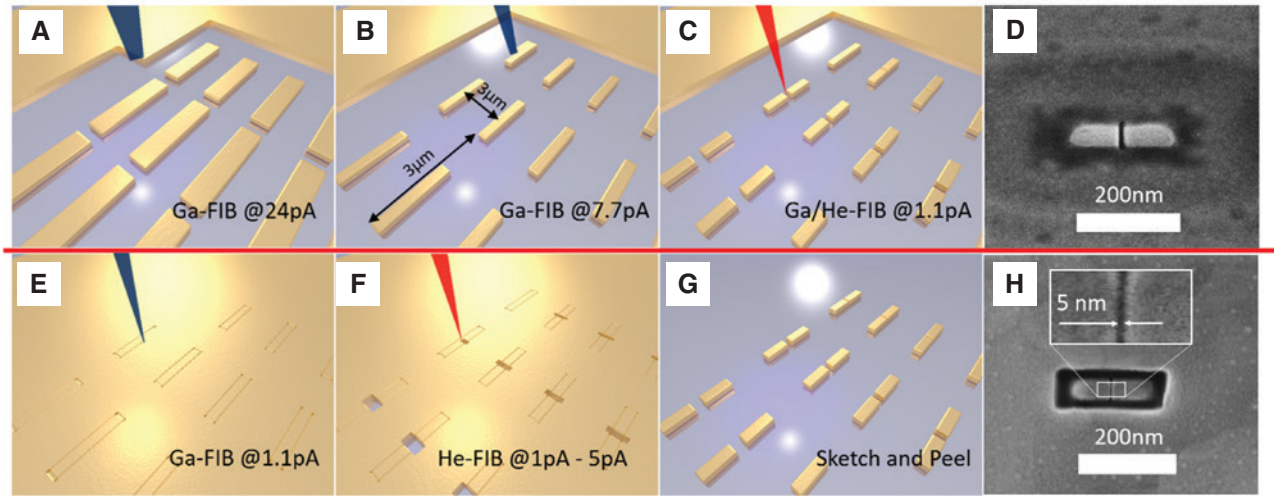

Figure 1: Schematics of the plasmonic nanorod dimer fabrication processes.
(A–C) Ga and Ga/He lithography to produce dimer antennas with gap distances of down to 6 nm. (D) Scanning electron micrograph of a single nanorod with a gap size of 6 nm. (E–G): sketch and peel (SaP)–based fabrication process. (E) The outline of the nanostructures is milled using a Ga^+-ion beam at low current. (F) In a second step, the He-FIB is used to fabricate gaps with distances of down to 5 nm. (G) An adhesive tape is used to selectively remove the outer regions of the nanostructure. (H) Helium-ion micrograph of a prototypical dimer antenna after the He-FIB process with a gap size of 5 nm before the SaP process.

confocal dark-field microscope. In the first two, gallium-based lithography strategies, the Ga^+-ion beam (blue) with a current of 24 pA, was used to remove most of the gold film (A), followed by a second step of Ga^+-ion beam writing at a current of 7.7 pA to outline the still-connected dimer nanorods (B). The dimers were finalized in a third step by cutting through the nanorods using either the Ga-FIB ("gallium lithography") or the He-FIB ("gallium/helium lithography") at a current of a few pA (C). Figure 1D shows a scanning electron micrograph of a prototypical nanorod dimer antenna with a gap distance of 6 nm. The three different fabrication steps (A–C) are visible by the different grey scales of the outer rim, the inner rim, and the gap region. Interestingly, charging effects of the dimer during the scanning electron microscope (SEM) image acquisition process were negligible, indicating that the first and second fabrication steps indeed induced doping of gallium or gold in the substrate.

The third fabrication strategy includes the much faster SaP strategy. Here, the contour of the desired nanostructure was milled into the metal film for 600 ms using the Ga-FIB (blue) at a current of 1.1 pA (Figure 1E). Subsequently, the He-FIB (red) was used at a current of 1 pA for 200 ms to split the antenna in half and fabricate gaps with gap sizes between 5 and 35 nm (F). Finally, a carbon-free, adhesive tape attached to the metal film was used to selectively peel the gold film outside the contoured area (G). In Figure 1H, a helium-ion micrograph of a prototypical antenna with a gap size of 5 nm is displayed, in which the high uniformity of the gap region becomes visible. Here, the gap size was taken as the FWHM of cross sections along high-resolution scanning electron and helium-ion micrographs (cf. Chapter S2 of the Supporting Information). The dimer antennas remained on the substrate because of the formation of a sidewall coating [52]. Here, charging effects of the sample during the image acquisition precluded high-resolution SEM images of isolated, stripped dimer antennas. However, low-magnification SEM and far-field optical microscope images of arrays of dimer antennas indeed prove the successful peeling process (cf. Chapter S3 of the Supporting Information).

2.2 Optical modelling

The linear optical response of the dimer antennas was simulated using a commercial software package, Lumerical FDTD Solutions. The 3D model system consisted of the gold dimer antenna on a fused silica substrate with the dimensions matching the same geometrical arrangement as the sample. The dielectric functions for gold were taken from Olmon et al. [53]. The fused silica substrate was modelled with an index of refraction of $n = 1.45$, and the whole structure was surrounded by vacuum. Perfectly matched layer boundary conditions were used on all sides of the calculation domain. A linearly polarized incident pulse with a Gaussian frequency spectrum was used to excite the sample. The polarisation was set along the long axis of the

antenna. The total simulation region was set to $(750\ \text{nm})^3$ with a spatially variable mesh size of down to 1 nm in the gap region The simulation region was chosen sufficiently large to avoid a near-field absorption at the boundaries of the simulation box.

2.3 Optical dark-field spectroscopy

Linearly polarized, ultra-broadband laser pulses from a coherent white light source (WLS) (Fianium SC-450-4) with a spectrum ranging from 450 nm to 2 µm with few-picosecond pulse duration and an average pulse energy of 60 pJ at 78 MHz repetition rate were collimated, spatially filtered, and focused to a rather large diameter of approximately 1.1 mm × 120 µm (FWHM) onto the sample at an angle of approximately 75°. The polarisation of the light was controlled using an ultra-broadband linear polarizer in combination with an achromatic half-wave plate. The incident polarisation is chosen along the long axis of the dimer in order to optimize the coupling to the optically bright bonding mode of the nanorod dimer [54–56]. The scattering spectrum of an isolated dimer was collected in reflection geometry using an extra-long working distance glass objective with a NA = 0.7 (Nikon, BD Plan 60x ELWD) and sent to a monochromator (Princeton Instruments, Acton SP2500) attached to an LN_2-cooled CCD camera (Princeton Instruments, SPEC10 100BR). By imaging the array of nanorod dimer antennas onto the CCD of the spectrometer, individual dimer antennas were selected. The position of the sample in the laser focus could be adjusted in all three dimensions with a manual three-axis linear actuator. A more detailed scheme of the experimental setup is given in Chapter S1 of the Supporting Information.

2.4 Linear scattering spectra

In Figure 2A, normalized linear scattering spectra of two prototypical dimer antennas fabricated using the SaP technique with gap distances of 24 and 6 nm are displayed as a blue dashed and a blue solid line, respectively. For light that is linearly polarized along the long axis of the dimer, these spectra display only a single peak, the optically bright, bonding mode of the dimer. This mode results from the coupling to the fundamental, LSPR of each nanorod. For nanorods with very similar geometries, the respective antibonding mode is optically dark. Higher-order LSPR resonances of the dimer lie on the short-wavelength side, outside the probed

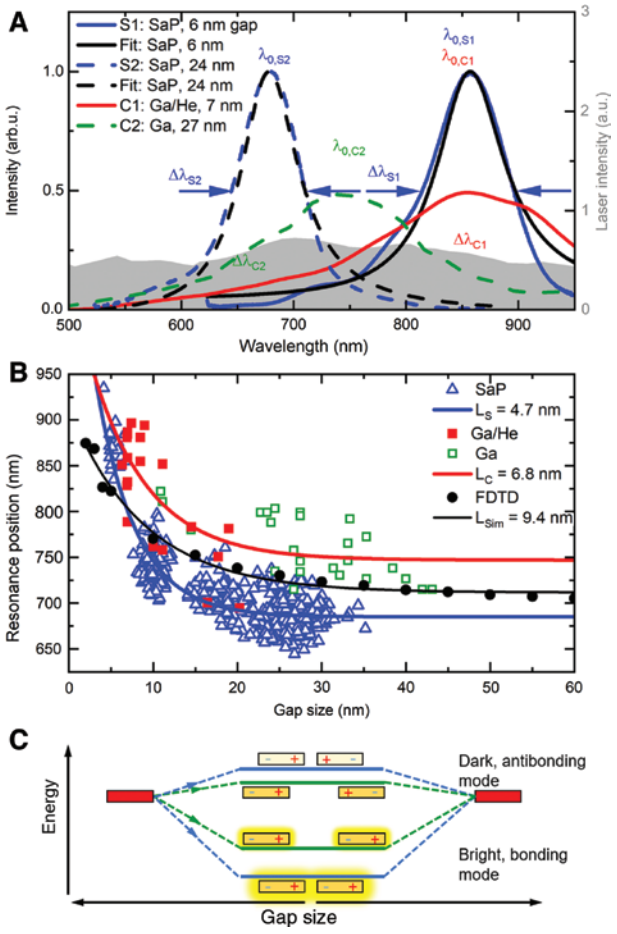

Figure 2: Resonance positions.
(A) Linear scattering spectra of prototypical dimer antennas with dimensions of $90 \times 35 \times 30\ \text{nm}^3$ fabricated using sketch and peel lithography (SaP, blue) with gap sizes of 6 nm (solid line) and 24 nm (dashed line), gallium (Ga, green, 27 nm), and gallium/helium (Ga/He, red, 7 nm) lithography. The black lines show Lorentzian line shape fits to the SaP scattering spectra. The spectrum of the excitation laser is shown as a grey-shaded background. (B) Resonance position λ_0 of dimer antennas fabricated using SaP (blue triangles), Ga (green squares), and Ga/He (red squares) as a function of gap size. Results from FDTD simulations (black circles) and from a quasi-static model (light-blue diamonds) are compared to exponential gap size dependencies of the resonance position with decay lengths of 4.7 nm (blue), 6.8 nm (red), and 9.4 nm (black). (C) Schematic energy-level diagram of the LSPR mode for dimer antennas with different gap sizes. A decrease in gap size (green and blue lines) results in a red shift of the bright, bonding mode.

spectral window, and for highly symmetric samples, the excitation of transverse SPR resonance is suppressed by the choice of incident polarisation. The measured spectral resonances are well described by single Lorentzian lineshapes, shown by a black dashed and a black solid line. The resonance wavelength $\lambda_{0,S2}$ of the dimer with a larger gap is 680 nm with an FWHM of approximately

$\Delta\lambda_{S2} = 64$ nm, whereas the resonance wavelength $\lambda_{0,S1}$ for the dimer with a 6-nm gap is 854 nm with $\Delta\lambda_{S1} = 81$ nm. Additionally, the linear scattering spectra of two dimer antennas with gaps of 7 nm (red solid line) and 27 nm (green dashed line), fabricated using Ga and Ga/He lithography technique, are presented. Here, the deduced resonance parameters are $\lambda_{0,C2} = 745$ nm ($\Delta\lambda_{C2} = 160$ nm) for the large-gap dimer and $\lambda_{0,C1} = 846$ nm ($\Delta\lambda_{C1} = 183$ nm) for the small-gap dimer. The spectrum of the exciting WLS is shown as a grey-shaded background.

Now, the resonance wavelengths of 46 fully Ga and Ga/He-fabricated and 560 SaP-fabricated dimer antennas of the same dimensions are compared in Figure 2B. Many more SaP-fabricated antennas could be tested as their fabrication is much faster and more accurate than for FIB milling. Here, open green and red squares denote the dimer antennas fabricated using the Ga and the Ga/He lithography, respectively, whereas open blue triangles represent the antenna produced by SaP. The superior milling precision of the He-FIB in the SaP procedure is apparent in the clustering of the dimer antennas around the designated gap sizes of 5 and 10 nm with standard deviations of 0.7 and 0.9 nm, respectively. The difference between the measured and nominal gap size of about 1 nm is independent of the fabrication technique and the nominal size (cf. Chapter S2 of the Supporting Information). The standard deviation of the gap size distributions for He^+-ion cutting of about 1 nm is approximately a factor of two lower than that for pure Ga^+ lithography.

As can be seen, all three distributions show a very similar behaviour: For gap sizes larger than approximately 20 nm, the resonance wavelength was constant around 750 nm for the Ga and Ga/He-produced and around 685 nm for the SaP-produced dimer antennas. The difference in resonance positions for the same geometries may be explained by a strongly increased Ga^+-ion doping and resputtering of Au of the substrate for the pure FIB approach compared to the outline procedure. This doping and redepositing are demonstrated by high-resolution secondary ion-mass spectrometry (NanoSIMS) measurements of the surrounding area of the dimer antenna (see Supporting Information Figure S5). Metal doping of glass leads to a higher refractive index [57] causing a red shift of the respective localized surface plasmon (LSP) modes [26]. It is seen in Figure 2B that the red shift between the Ga/He and SaP decreases for smaller gap sizes. We believe that this is clear signature of the improved fabrication quality of the SaP antennas. For the same gap distance, we observe a stronger coupling-induced red shift of the dimer resonance for the SaP antennas than for the Ga/He, implying that the improvement in fabrication quality enhances the field localisation in the gap region and thus the coupling between the two antenna arms. Furthermore, the superior fabrication quality of the SaP approach becomes especially visible for smaller gap sizes. Here, the distribution of the resonance positions of the dimers is narrower, suggesting accordingly smaller geometrical imperfections.

For decreasing gap sizes, however, the resonance position red shifted significantly to 895 nm for all three fabrication processes by nearly $\delta\lambda = 150$ nm for the Ga and Ga/He-produced and by more than $\delta\lambda = 210$ nm for the SaP-produced nanorod dimer antennas. The optical near-field coupling between the two LSPR resonances of the two nanorods results in the formation of a red-shifted, delocalized bonding mode of the dimer. The fractional red shift of the LSPR resonance that is seen in Figure 2B amounts to up to $\delta\lambda/\lambda_0 = 0.31$, even larger than values reported for chemically synthesized nanorods with gap distances around 3 to 4 nm [58]. This large red shift, however, occurs only for gap sizes below 20 nm and can – with some limitations – be well approximated by exponential decay fits, known as the universal plasmon ruler equation [56, 59, 60] $\Delta\lambda/\lambda_0 = a \cdot \exp(-d_{gap}/l)$ with a being a constant and d_{gap} the gap size. The exponential decay fits are shown in Figure 2B by the red (Ga and Ga/He lithography) and blue (SaP) lines with decay length of $L_C = 6.8$ nm and $L_S = 4.7$ nm, respectively.

In comparison to the experimental data, the resonance positions extracted from scattering spectra simulated using a Maxwell equations solver (FDTD solutions) are shown by black circles with an exponential decay length of $L_{Sim} = 9.4$ nm (black solid line). These decay lengths are similar to those simulated for a metallic nanoparticle dimer on a mirror configuration [61] but significantly shorter than the decay lengths of approximately 20 to 30 nm that have been reported for ellipsoid nanoparticles [56] and predicted for chemically synthesized nanorods [58]. As it was pointed out by Dolinnyi [60], large deviations from the plasmon ruler equation are expected to occur for few-nanometer interparticle distances, and hence a biexponential may be more suitable. The observed increasing red shift for decreasing gap sizes is a clear signature of a near-field induced coupling of the two dimer arms [27, 56, 62, 63], resulting in mode splitting of the uncoupled LSPR mode of the individual rods into a dark, i.e. far-field invisible, slightly blue-shifted (antibonding) and a bright, (bonding) red-shifted mode [27, 28, 64]. This mode splitting is indicated by the energy-level diagram in Figure 2C, where the formation of a bright, bonding mode and a dark, antibonding mode from the LSP mode of uncoupled nanorods (red rectangles) is

sketched for two dimers with different gap sizes (green and blue dashed lines).

Next, we compare the quality factors Q of the bright, bonding mode of nanorod dimer antennas produced by the three fabrication processes. Here, the quality factor is defined as the ratio of the resonance frequency ω_0 and the twice the damping constant γ, i.e. $Q=\omega_0/2\gamma$, or $Q=\lambda_0/\Delta\lambda_{FWHM}$. This quality factor is a measure for the dephasing time $T_2=1/\gamma$ of the electric field emitted by the antenna, i.e. the decay of the coherent polarisation within the gap region of the nanorod dimer antenna due to radiative and Ohmic damping [65, 66]. The dephasing time thus determines the number of oscillation cycles of the free-induction decay of the SP oscillations [67] and is directly proportional to the field enhancement factor, i.e. the ratio between local field at the sample surface and incident field [68]. This is of special interest when studying the coupling between the LSP mode and a quantum emitter placed in the spot of the gap antenna. When the emitter is weakly coupled to the LSP mode, a high Q and a small mode volume V in between the dimer antenna arms both increase the Purcell factor $F_P \sim Q/V$, giving the enhancement of the spontaneous emission of the emitter beyond its vacuum value [33, 69]. Such high Q factors are of particular interest as they result in a small damping γ_{LSP} of the antenna mode while enhancing vacuum field fluctuations in the gap. This is of key importance for reaching the strong-coupling regime, $\Omega_R^2 > \gamma_{LSP}^2/2 + \gamma_{QE}^2/2$, in which the strength of the emitter-plasmon coupling Ω_R exceeds the sum of the dephasing rates of the QE and LSP mode [16, 33, 70]. This regime can result in a periodic exchange of energy between LSP mode and emitter on a femtosecond time scale [71].

In Figure 3, the quality factor Q (A) and the dephasing time T_2 (B) of the LSPR resonance of dimer antennas fabricated by the three techniques are displayed as a function of the gap distance. Again, open green and red squares represent antennas fabricated by Ga and Ga/He lithography, respectively, and open blue triangles show the SaP antennas. The black circles denote Q factors and T_2 times

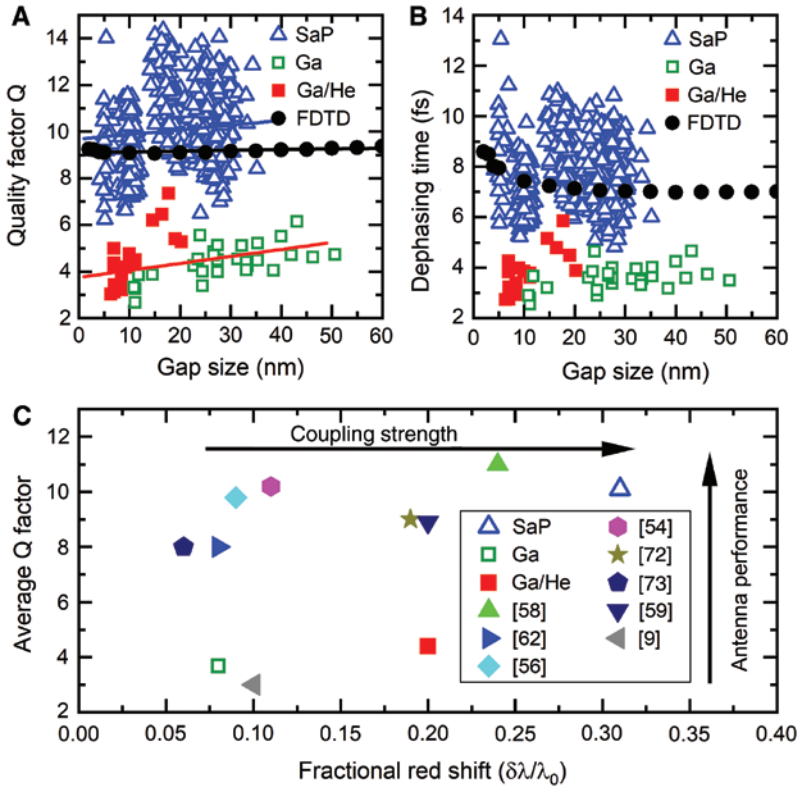

Figure 3: Nanorod dimer antennas performance.
(A) Quality factor Q of the dimer antennas fabricated using SaP (blue triangles), Ga (green squares), and Ga/He (red squares) as a function of gap size. Results from FDTD simulations are shown as black circles. The lines are guides to the eye. (B) Dephasing time T_2 of the electric field of the antennas. (C) Comparative analysis of quality factors Q and fractional red shifts $\delta\lambda/\lambda_0$ of dimer antennas fabricated using different chemical synthesis and lithography techniques. SaP allows one to fabricate strongly coupled antennas with high-quality factors.

of the simulated resonances. Solid lines in the respective colours are given as guides to the eye. Now, the Q factors for all Ga and Ga/He-fabricated structures are between 2.5 and 7 with an average value of 4.4. The Q factors of the SaP dimer antennas in contrast are significantly larger, ranging from about 6 to a maximum Q factor of 14.4. The average value for the SaP antennas is 10.1, even slightly larger than the average Q factor of 9.2 obtained from FDTD simulations. The quality factors for the SaP-produced dimer antennas are also larger than those reported for dimer antennas of similar size that were chemically synthesized [58, 74], fabricated using EBL [54, 72, 73] and Ga-FIB [20], and also higher than those reported earlier for SaP-produced circular dimers [52]. Even more, the quality factor approaches values that so far have been reached only for single-crystalline chemically synthesized single linear rods, for which, however, the field localisation is significantly smaller [65]. For some of our SaP dimer antennas, we reach Q factors that are similar to those reported for encapsulated and annealed single nanorods [3]. This again demonstrates the high fabrication quality of the SaP process that results in dephasing times longer than 10 fs, as can be seen in Figure 3B.

As both, the fractional red shift as an indicator for the field enhancement, and the quality factor Q as a measure for the storage time of electric field inside the dimer antennas are the relevant quantities for the antenna design, the two parameters are plotted in two-dimensional distribution in Figure 3C and are compared to literature values. As can be seen, the fabricated dimer antennas using the SaP approach are located on the upper right corner, indicating their superior ability to concentrate electromagnetic fields to nanometer dimensions for significantly long times.

To confirm that we indeed probe the longitudinal SPR of the dimer antenna alone, we have performed detailed polarisation-sensitive measurements of isolated SaP-produced nanorod dimer antennas with gap sizes of 5 and 25 nm, shown in Figure 4A. Here, the scattering spectra are displayed for a small-gap (solid lines) and a large-gap (dashed line) dimer for varying polarisation angles of θ of the linearly polarized incident light. The polarisation angle is defined as the angle between electric field vector and long axis of the nanorod dimer. The angle-dependent, spectrally-integrated intensity for the dimer with 5-nm gap size is shown in (B) as a polar plot as green squares together with a $\cos^2(\theta)$ fit (black line) to the experimental data. The spectra indicate that for the light being polarized along the connection axis of the two nanorods antennas ($\theta = 0°$), mainly the longitudinal, red-shifted resonance of the dimer antenna with a small gap

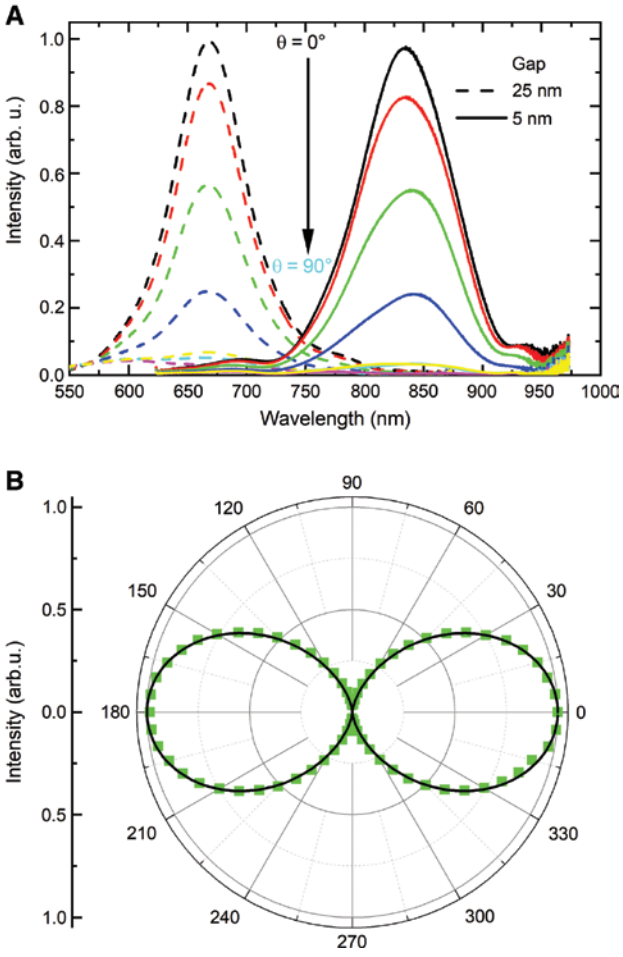

Figure 4: Polarisation dependence of the LSPR.
(A) Polarisation-resolved linear scattering spectra recorded from SaP dimer antennas with gaps of 5 nm (solid lines) and 25 nm (dashed line) for different polarisation angles θ at linearly polarized excitation laser. (B) Angular plot of the spectrally integrated intensity (green squares) of the SaP dimer with a gap size of 5 nm together with a $\cos^2(\theta)$ fit (black line).

is excited. This resonance shifts to smaller wavelengths for increasing gap sizes as can be seen for the large gap size, indicated by the dashed lines. The suppression ratio, i.e. the ratio of spectrally-integrated intensity at the single resonance with the light being polarized along the long axis compared to light polarized perpendicular to the long axis, is around 90:1 for the 5-nm gap and 85:1 for the 25-nm gap. This again underlines the high structural quality of our SaP antennas.

Our experimental findings indirectly evidence the strong coupling and hence high field localisation in the gap region of the two antenna arms. To further support this assertion, we compared our experimental results to three-dimensional FDTD simulations of the dimer antenna spectra. In Figure 5A, the simulated linear

scattering spectra (dashed lines, left *y*-axis) are compared to normalized experimental spectra (right *y*-axis) of SaP dimers with varying gap sizes. Both resonance position and the spectral line shape are fairly well reproduced in the simulation, even though the red shift for the 5-nm gap sizes is still underestimated in the simulations. We ascribe this to an imperfect, since unknown matching of the simulated dimer antenna geometries to those in the experiment. In Chapter S4 of the Supporting Information, we further compare the scattering intensity $P = \int I(\lambda) d(\lambda)$ of the simulated and the experimental nanorod dimer antennas. This shows that for decreasing gap size the measured scattered signals increases slightly, just as it is also visible in the increase of the scattering cross section in the simulation.

To illustrate the coupling of the two antenna arms in more detail, Figure 5B shows the colour-coded field enhancement factor $L_{res}(x,y) = <|E_x(x,y,z=20\,\text{nm})|>/<|E_0|>$ at nearly half height for two different gap distances of 5 nm (left) and 25 nm (right) at the resonance wavelengths

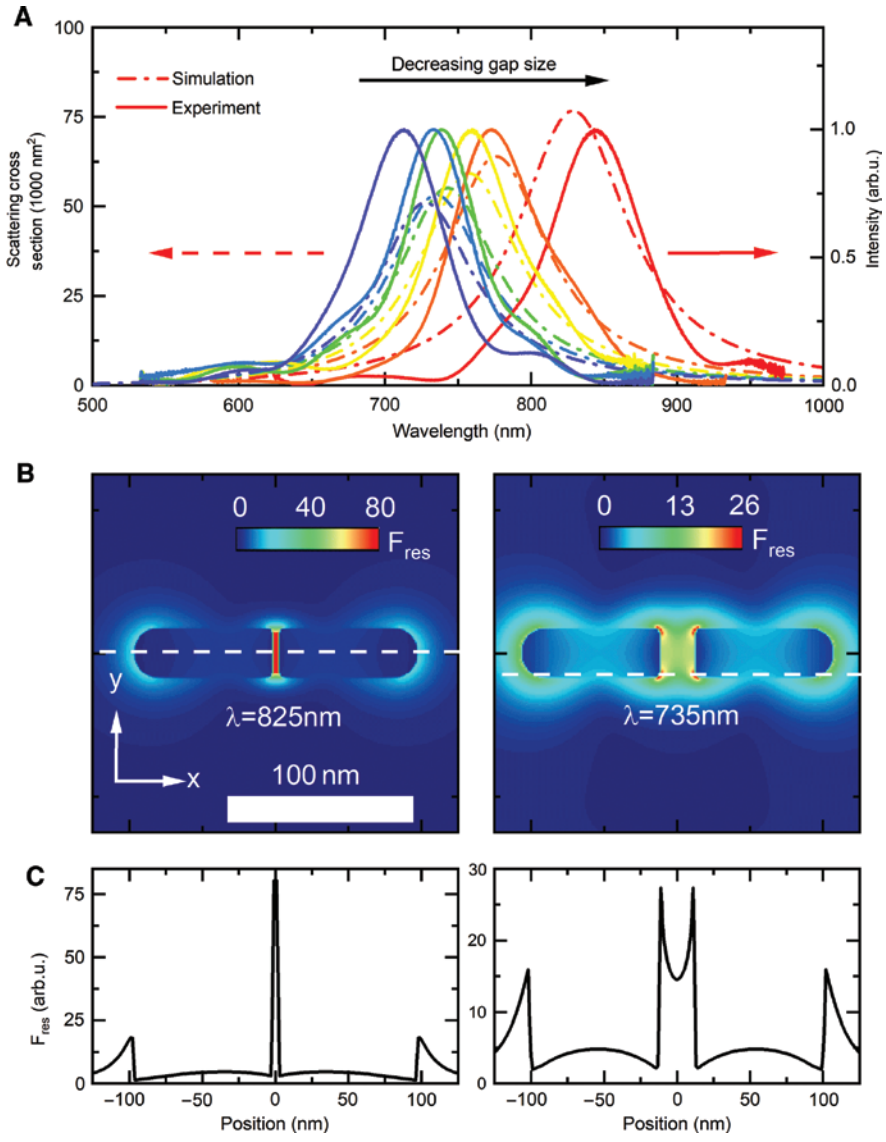

Figure 5: Comparison of experiment and FDTD Simulaton.
(A) Experimentally measured, normalized (right *y*-axis, solid lines), and simulated (left axis, dashed lines) scattering spectra of SaP dimer antennas with gap sizes varying between 5 and 30 nm (red to blue colours). (B) Calculated near-field distributions of gold dimer antennas in the *x*-*y* plane for a gap size of 5 nm (left) and 25 nm (right). The colour code displays the local near-field enhancement $F_{res}(x, y) = <|E_x(x, y, z=20\,\text{nm})|>/<|E_0|>$ at the resonance wavelengths of 825 nm (left) and 735 nm (right) as indicated in the panel. (C) Cross-cut of the local near-field enhancement along the *x*-axis at the white dashed line (B).

of 825 and 735 nm, respectively. In Figure 5C, cross-cuts of F_{res} along the x-axis at the white dashed line in (B) are shown for the two respective gap sizes. As can be seen, the electric field for the 25-nm gap is concentrated at the corners of the structure, reaching $F_{res}=28$. However, the field decays already in the gap region due to the larger gap of 25 nm. For the 5-nm gap, the field is concentrated exclusively in the gap region, where a spatially homogenous, capacitor-like electric field distribution is created, reaching a maximum field enhancement factor F of 81. This spatially homogeneous electric near field in the gap is excellently suited for coupling the plasmon field to that of a quantum emitter sample positioned inside the gap.

3 Conclusion

The combination of Ga^+- and He^+-ion beam lithography with a novel SaP technique provides a high, few-nanometer precision for the fabrication of isolated, nanometer-sized plasmonic particles. We have used this technique to fabricate nanorod dimer antennas of 2×90-nm length from a 30-nm-thick gold substrate with varying gap sizes down to 5 nm. By using linear, polarisation-resolved dark-field spectro-microscopy, the ability of these structures to confine electromagnetic fields in their gap region was probed. We took the linear response, i.e. the red shift of the optically bright bonding mode and the quality factor of the nanorod dimer antennas as a measure for the field localisation in the gap region. The SaP-produced dimers were compared to dimer antennas fabricated using a standard Ga-FIB and He-FIB lithography approach. We find an enormous red shift for the SaP-produced dimers of more than $\delta\lambda/\lambda_0=0.31$, larger than those reported for chemically synthesized nanorods [58] and those fabricated using EBL [59]. The average quality factor $Q=\lambda_0/\Delta\lambda$ of the SaP-produced dimers exceeded 10, more than a factor of two larger compared to the conventionally fabricated rods using EBL or Ga-FIB. Finite-difference time-domain simulations of the linear scattering spectrum and the electric field confined in the gap region support our conclusion that by using the presented fabrication technique nanorod dimer antennas with superior fabrication quality and the ability to concentrate light into nanometer dimensions could be produced. Our results suggest that the improvement in fabrication quality will not only affect the near- and far-field radiation pattern of the nanorod dimers but may also lead to a significant enhancement of their nonlinear optical efficiency. Experimental studies of these properties are currently underway. We anticipate that the presented technique can be a cornerstone for the fabrication of complex plasmonic nanostructures, where the interaction of localized plasmon and propagating surface plasmon polariton waves with excitonic materials is probed on nanometer dimensions [34].

In the present work, we have discussed the red shift of the dimer SP resonance in terms of the hybridisation model introduced in Ref. [28]. This classical coupled-dipole model predicts three distinct signatures of a strong coupling between the two rods of a dimer: (A) the appearance of two energetically split, hybrid SP resonances of the dimer: a symmetric, optically bright mode and an antisymmetric, optically dark mode; (B) an increase in radiative damping of the bright mode and a decrease in radiative damping of the dark mode (as opposed to that of the individual rods); (C) an increased (decreased) scattering cross section (effective dipole moment) of the bright (dark) mode in comparison to that of the individual rods [75]. The strong coupling regime is reached when the energetic splitting between the coupled resonances exceeds the linewidth of the uncoupled resonances [33, 76, 77]. We have taken the observed red shift of the dimer resonance of up to 450 meV (Figure 2B), much larger than the FWHM of the dimer resonance for large gap distances (170 meV, Figure 2A) as the distinct signature of strong coupling in our antennas. Two more features in the far-field optical spectra of such dimers may be taken as additional indications for strong coupling: (A) the change in radiative linewidth and (B) the change in the ratio between scattering and absorption cross section of the dimer resonance with coupling strength, i.e. with decreasing gap size. Both quantities are more difficult to analyse than the spectral shift of the dimer resonance as also nonradiative damping contributes significantly to the lineshape. A more in-depth analysis of the effect of the gap distance on the linewidth and on the ratio between absorption and scattering cross sections [78] might reveal additional insight into coupled dimer antennas. In principle, additional information on the coupling between the antenna arms may also be deduced by analysing the optical properties of antisymmetric dark mode [79], either by asymmetric far-field optical excitation schemes [79], electron energy loss spectroscopy, or near-field optical spectroscopy. In our far-field experiments, we did not find clear signatures of this dark mode, implying that the optical properties of two coupled rods are too similar to result in a significant oscillator strength of the dark mode.

An alternative signature of strong coupling in such nanodimer antennas is the periodic, oscillatory exchange of energy between the two coupled rods, mediated by their near-field coupling [33, 34, 77]. In order to probe these dynamic couplings, it is necessary to locally excite

one of the rods with an optical pulse that is shorter in duration than the Rabi period, i.e. the time it takes for the energy to oscillate between the two arms of the antenna. This oscillatory energy transfer is a distinct manifestation of strong coupling in coupled nanosystems. Due to the short time and small length scales involved, such experiments are challenging and have so far reported only very few selected hybrid systems [33, 34, 77]. Importantly, the signatures of such strong couplings in the linear optical regime are identical in classical coupled dipole models, systems of two coupled quantum-mechanical harmonic oscillators, and for two-level systems coupled to plasmonic harmonic oscillator modes (Jaynes–Cummings model). Nonlinear experiments are therefore needed to reveal the quantum signatures of strong coupling.

Acknowledgements: Financial support by the Deutsche Forschungsgemeinschaft (SPP 1840 and GRK 1885) (SPP 1839, Funder Id: http://dx.doi.org/10.13039/501100001659 and SPP1840) and the Korea Foundation for International Cooperation of Science and Technology (Global Research Laboratory project, K20815000003). M.S. wishes to thank the BMBF for a personal research grant "Photonic Transistors" in the NanoMatFutur program, Funder Name: Bundesministerium für Bildung und Forschung, Funder Id: http://dx.doi.org/10.13039/501100002347, Grant Number: NanoMatFutur FKZ: 13N13637. The He ion beam patterning was performed in the Corelab Correlative Microscopy and Spectroscopy at Helmholtz-Zentrum Berlin.

Conflicts of interest: There are no conflicts to declare.

Author information: M.G. built up the optical setup and performed the optical experiments, together with H.K. The samples were produced by M.G., H.K., and K.H. The data were analysed by M.G. and M.S. C.L. and M.S. initiated the experiment. FDTD simulations were performed by V.S. and M.G. together with M.S. The manuscript was written by M.S. with contributions from all authors. All authors have given approval to the final version of the manuscript.

References

[1] Schuck PJ, Fromm DP, Sundaramurthy A, Kino GS, Moerner WE. Improving the mismatch between light and nanoscale objects with gold bowtie nanoantennas. Phys Rev Lett 2005;94:017402.
[2] Knittel V, Fischer MP, de Roo T, Mecking S, Leitenstorfer A, Brida D. Nonlinear photoluminescence spectrum of single gold nanostructures. ACS Nano 2015;9:894–900.
[3] Bosman M, Zhang L, Duan H, et al. Encapsulated annealing: enhancing the plasmon quality factor in lithographically-defined nanostructures. Sci Rep 2014;4:5537.
[4] Butet J, Brevet P-F, Martin OJF. Optical second harmonic generation in plasmonic nanostructures: from fundamental principles to advanced applications. ACS Nano 2015;9:10545–62.
[5] Yoo K, Becker Simon F, Silies M, Yu S, Lienau C, Park N. Steering second-harmonic radiation through local excitations of plasmon. Opt Exp 2019;27:18246–61.
[6] Bouhelier A, Beversluis M, Hartschuh A, Novotny L. Near-field second-harmonic generation induced by local field enhancement. Phys Rev Lett 2003;90:013903.
[7] Aouani H, Navarro-Cia M, Rahmani M, et al. Multiresonant broadband optical antennas as efficient tunable nanosources of second harmonic light. Nano Lett 2012;12:4997–5002.
[8] Celebrano M, Wu X, Baselli M, et al. Mode matching in multiresonant plasmonic nanoantennas for enhanced second harmonic generation. Nat Nanotechnol 2015;10:412–7.
[9] Kollmann H, Piao X, Esmann M, et al. Toward plasmonics with nanometer precision: nonlinear optics of helium-ion milled gold nanoantennas. Nano Lett 2014;14:4778–84.
[10] Lippitz M, van Dijk MA, Orrit M. Third-harmonic generation from single gold nanoparticles. Nano Lett. 2005;5:799–802.
[11] Metzger B, Hentschel M, Lippitz M, Giessen H. Third-harmonic spectroscopy and modeling of the nonlinear response of plasmonic nanoantennas. Opt Lett 2012;37:4741–3.
[12] Hanke T, Krauss G, Träutlein D, Wild B, Bratschitsch R, Leitenstorfer A. Efficient nonlinear light emission of single gold optical antennas driven by few-cycle near-infrared pulses. Phys Rev Lett 2009;103:257404.
[13] Ropers C, Solli DR, Schulz CP, Lienau C, Elsaesser T. Localized multiphoton emission of femtosecond electron pulses from metal nanotips. Phys Rev Lett 2007;98:043907.
[14] Vogelsang J, Robin J, Nagy BJ, et al. Ultrafast electron emission from a sharp metal nanotaper driven by adiabatic nanofocusing of surface plasmons. Nano Lett 2015;15:4685–91.
[15] Punj D, Mivelle M, Moparthi SB, et al. A plasmonic 'antenna-in-box' platform for enhanced single-molecule analysis at micromolar concentrations. Nat Nanotechnol 2013;8:512–6.
[16] Chikkaraddy R, de Nijs B, Benz F, et al. Single-molecule strong coupling at room temperature in plasmonic nanocavities. Nature 2016;535:127–30.
[17] Stockman MI. Nanofocusing of optical energy in tapered plasmonic waveguides. Phys Rev Lett 2004;93:137404.
[18] Vogelsang J, Talebi N, Hergert G, et al. Plasmonic-nanofocusing-based electron holography. ACS Photon 2018;5:3584–93.
[19] Melchior P, Bayer D, Schneider C, et al. Optical near-field interference in the excitation of a bowtie nanoantenna. Phys Rev B 2011;83:235407.
[20] Hanke T, Cesar J, Knittel V, et al. Tailoring spatiotemporal light confinement in single plasmonic nanoantennas. Nano Lett 2012;12:992–6.
[21] Fischer H, Martin OJF. Engineering the optical response of plasmonic nanoantennas. Opt Express 2008;16:9144–54.
[22] Schuller JA, Barnard ES, Cai W, Jun YC, White JS, Brongersma ML. Plasmonics for extreme light concentration and manipulation. Nat Mater 2010;9:193–204.
[23] Mühlschlegel P, Eisler H-J, Martin OJF, Hecht B, Pohl DW. Resonant optical antennas. Science 2005;308:1607–9.
[24] Metzger B, Hentschel M, Schumacher T, et al. Doubling the efficiency of third harmonic generation by positioning ito

nanocrystals into the hot-spot of plasmonic gap-antennas. Nano Lett 2014;14:2867–72.
[25] Osberg KD, Rycenga M, Harris N, et al. Dispersible gold nanorod dimers with sub-5 nm gaps as local amplifiers for surface-enhanced Raman scattering. Nano Lett 2012;12:3828–32.
[26] Biagioni P, Huang J-S, Hecht B. Nanoantennas for visible and infrared radiation. Rep Prog Phys 2012;75:024402.
[27] Huang J-S, Kern J, Geisler P, et al. Mode imaging and selection in strongly coupled nanoantennas. Nano Lett 2010;10:2105–10.
[28] Prodan E, Radloff C, Halas NJ, Nordlander P. A hybridization model for the plasmon response of complex nanostructures. Science 2003;302:419–22.
[29] Chu M-W, Myroshnychenko V, Chen CH, Deng J-P, Mou C-Y, García de Abajo FJ. Probing bright and dark surface-plasmon modes in individual and coupled noble metal nanoparticles using an electron beam. Nano Lett 2009;9:399–404.
[30] Jain PK, Eustis S, El-Sayed MA. Plasmon coupling in nanorod assemblies: optical absorption, discrete dipole approximation simulation, and exciton-coupling model. J Phys Chem B 2006;110:18243–53.
[31] Duan H, Fernández-Domínguez AI, Bosman M, Maier SA, Yang JKW. Nanoplasmonics: classical down to the nanometer scale. Nano Lett 2012;12:1683–9.
[32] Willingham B, Brandl DW, Nordlander P. Plasmon hybridization in nanorod dimers. Appl Phys B 2008;93:209–16.
[33] Vasa P, Lienau C. Strong light–matter interaction in quantum emitter/metal hybrid nanostructures. ACS Photonics 2018;5:2–23.
[34] Vasa P, Wang W, Pomraenke R, et al. Real-time observation of ultrafast Rabi oscillations between excitons and plasmons in metal nanostructures with J-aggregates. Nat Photonics 2013;7:128–32.
[35] Readman C, de Nijs B, Szabó I, et al. Anomalously large spectral shifts near the quantum tunnelling limit in plasmonic rulers with subatomic resolution. Nano Lett 2019;19:2051–8.
[36] Liu B, Chen S, Zhang J, et al. A plasmonic sensor array with ultrahigh figures of merit and resonance linewidths down to 3 nm. Adv Mater 2018;30:e1706031.
[37] Rai-Choudhury P. Handbook of microlithography, micromachining, and microfabrication. London, UK, Institution of Engineering and Technology, 1997.
[38] Hu H, Duan H, Yang JKW, Shen ZX. Plasmon-modulated photoluminescence of individual gold nanostructures. ACS Nano 2012;6:10147–55.
[39] Dodson S, Haggui M, Bachelot R, Plain J, Li S, Xiong Q. Optimizing electromagnetic hotspots in plasmonic bowtie nanoantennae. J Phys Chem Lett 2013;4:496–501.
[40] Liu K, Avouris P, Bucchignano J, Martel R, Sun S, Michl J. Simple fabrication scheme for sub-10 nm electrode gaps using electron-beam lithography. Appl Phys Lett 2002;80:865–7.
[41] Kim S, Jin J, Kim Y-J, Park I-Y, Kim Y, Kim S-W. High-harmonic generation by resonant plasmon field enhancement. Nature 2008;453:757–60.
[42] Sivis M, Duwe M, Abel B, Ropers C. Nanostructure-enhanced atomic line emission. Nature 2012;485:E1–2.
[43] Volkert CA, Minor AM. Focused ion beam microscopy and micromachining. MRS Bull 2007;32:389–99.
[44] Huang J-S, Callegari V, Geisler P, et al. Atomically flat single-crystalline gold nanostructures for plasmonic nanocircuitry. Nat Commun 2010;1:150.
[45] Lindquist NC, Nagpal P, McPeak KM, Norris DJ, Oh S-H. Engineering metallic nanostructures for plasmonics and nanophotonics. Rep Prog Phys 2012;75:036501.
[46] Han G, Weber D, Neubrech F, et al. Infrared spectroscopic and electron microscopic characterization of gold nanogap structure fabricated by focused ion beam. Nanotechnology 2011;22:275202.
[47] Sidorkin V, van Veldhoven E, van der Drift E, Alkemade P, Salemink H, Maas D. Sub-10-nm nanolithography with a scanning helium beam. J Vac Sci Technol B Microelectron Nanometer Struct Process Meas Phenom 2009;27:L18–20.
[48] Chen K, Razinskas G, Vieker H, et al. High-Q, low-mode-volume and multiresonant plasmonic nanoslit cavities fabricated by helium ion milling. Nanoscale 2018;10:17148–55.
[49] Wang Y, Abb M, Boden SA, Aizpurua J, de Groot CH, Muskens OL. Ultrafast nonlinear control of progressively loaded, single plasmonic nanoantennas fabricated using helium ion milling. Nano Lett 2013;13:5647–53.
[50] Notte JA. Charged particle microscopy: why mass matters. Micros Today 2012;20:16–22.
[51] Tan S, Livengood R, Shima D, Notte J, McVey S. Gas field ion source and liquid metal ion source charged particle material interaction study for semiconductor nanomachining applications. J Vac Sci Technol B 2010;28:C6F15–16F21.
[52] Chen Y, Bi K, Wang Q, et al. Rapid focused ion beam milling based fabrication of plasmonic nanoparticles and assemblies via "Sketch and Peel" strategy. ACS Nano 2016;10:11228–36.
[53] Olmon RL, Slovick B, Johnson TW, et al. Optical dielectric function of gold. Phys Rev B 2012;86:235147.
[54] Rechberger W, Hohenau A, Leitner A, Krenn JR, Lamprecht B, Aussenegg FR. Optical properties of two interacting gold nanoparticles. Opt Commun 2003;220:137–41.
[55] Tamaru H, Kuwata H, Miyazaki HT, Miyano K. Resonant light scattering from individual Ag nanoparticles and particle pairs. Appl Phys Lett 2002;80:1826–8.
[56] Su KH, Wei QH, Zhang X, Mock JJ, Smith DR, Schultz S. Interparticle coupling effects on plasmon resonances of nanogold particles. Nano Lett 2003;3:1087–90.
[57] Gunawardena DS, Mat-Sharif KA, Tamchek N, et al. Photosensitivity of gallium-doped silica core fiber to 193 nm ArF excimer laser. Appl Opt 2015;54:5508–12.
[58] Funston AM, Novo C, Davis TJ, Mulvaney P. Plasmon coupling of gold nanorods at short distances and in different geometries. Nano Lett 2009;9:1651–8.
[59] Tabor C, Van Haute D, El-Sayed MA. Effect of orientation on plasmonic coupling between gold nanorods. ACS Nano 2009;3:3670–8.
[60] Dolinnyi AI. Nanometric rulers based on plasmon coupling in pairs of gold nanoparticles. J Phys Chem C 2015;119:4990–5001.
[61] Huang Y, Ma L, Hou M, Li J, Xie Z, Zhang Z. Hybridized plasmon modes and near-field enhancement of metallic nanoparticle-dimer on a mirror. Sci Rep 2016;6:30011.
[62] Muskens OL, Giannini V, Sánchez-Gil JA, Gómez Rivas J. Optical scattering resonances of single and coupled dimer plasmonic nanoantennas. Opt Express 2007;15:17736–46.
[63] Gunnarsson L, Rindzevicius T, Prikulis J, et al. Confined plasmons in nanofabricated single silver particle pairs: experimental observations of strong interparticle interactions. J Phys Chem B 2005;109:1079–87.

[64] Nordlander P, Prodan E. Plasmon hybridization in nanoparticles near metallic surfaces. Nano Lett 2004;4:2209–13.
[65] Sönnichsen C, Franzl T, Wilk T, et al. Drastic reduction of plasmon damping in gold nanorods. Phys Rev Lett 2002;88:077402.
[66] Kim DS, Hohng SC, Malyarchuk V, et al. Microscopic origin of surface-plasmon radiation in plasmonic band-gap nanostructures. Phys Rev Lett 2003;91:143901.
[67] Stockman MI, Shahbazyan TV. Plasmonics: theory and applications. Dordrecht, Springer, 2013.
[68] Anderson A, Deryckx KS, Xu XG, Steinmeyer G, Raschke MB. Few-femtosecond plasmon dephasing of a single metallic nanostructure from optical response function reconstruction by interferometric frequency resolved optical gating. Nano Lett 2010;10:2519–24.
[69] Gérard JM, Sermage B, Gayral B, Legrand B, Costard E, Thierry-Mieg V. Enhanced spontaneous emission by quantum boxes in a monolithic optical microcavity. Phys Rev Lett 1998;81:1110–3.
[70] Baranov DG, Wersäll M, Cuadra J, Antosiewicz TJ, Shegai T. Novel nanostructures and materials for strong light–matter interactions. ACS Photonics 2018;5:24–42.
[71] Schlather AE, Large N, Urban AS, Nordlander P, Halas NJ. Near-field mediated plexcitonic coupling and giant Rabi splitting in individual metallic dimers. Nano Lett 2013;13:3281–6.
[72] Fromm DP, Sundaramurthy A, Schuck PJ, Kino G, Moerner WE. Gap-dependent optical coupling of single "Bowtie" nanoantennas resonant in the visible. Nano Lett 2004;4:957–61.
[73] Jain PK, Huang W, El-Sayed MA. On the universal scaling behavior of the distance decay of plasmon coupling in metal nanoparticle pairs: a plasmon ruler equation. Nano Lett 2007;7:2080–8.
[74] Kumar J, Wei X, Barrow S, Funston AM, Thomas KG, Mulvaney P. Surface plasmon coupling in end-to-end linked gold nanorod dimers and trimers. Phys Chem Chem Phys 2013;15:4258–64.
[75] Dahmen C, Schmidt B, von Plessen G. Radiation damping in metal nanoparticle pairs. Nano Lett 2007;7:318–22.
[76] Thompson RJ, Rempe G, Kimble HJ. Observation of normal-mode splitting for an atom in an optical cavity. Phys Rev Lett 1992;68:1132–5.
[77] Torma P, Barnes WL. Strong coupling between surface plasmon polaritons and emitters: a review. Rep Prog Phys 2015;78:1–34.
[78] Husnik M, Linden S, Diehl R, Niegemann J, Busch K, Wegener M. Quantitative experimental determination of scattering and absorption cross-section spectra of individual optical metallic nanoantennas. Phys Rev Lett 2012;109:233902.
[79] Huang JS, Kern J, Geisler P, et al. Mode imaging and selection in strongly coupled nanoantennas. Nano Lett 2010;10:2105–10.

Supplementary Material: The online version of this article offers supplementary material (https://doi.org/10.1515/nanoph-2019-0379).